

Article

# An Atmospheric Correction Using High Resolution Numerical Weather Prediction Models for Satellite-Borne Single-Channel Mid-Wavelength and Thermal Infrared Imaging Sensors

Hongtak Lee <sup>1,2</sup>, Joong-Sun Won <sup>2</sup>  and Wook Park <sup>2,\*</sup>

<sup>1</sup> Satellite Application Division, Satellite Operation and Application Center, Korea Aerospace Research Institute, Daejeon 34133, Korea; leeht@kari.re.kr

<sup>2</sup> Department of Earth System Science, Yonsei University, Seoul 03722, Korea; jswon@yonsei.ac.kr

\* Correspondence: pw1983@yonsei.ac.kr; Tel.: +82-2123-2673

Received: 30 December 2019; Accepted: 4 March 2020; Published: 6 March 2020



**Abstract:** This paper presents a single-channel atmospheric correction method for remotely sensed infrared (wavelength of 3–15  $\mu\text{m}$ ) images with various observation angles. The method is based on basic radiative transfer equations with a simple absorption-focused regression model to calculate the optical thickness of each atmospheric layer. By employing a simple regression model and re-organization of atmospheric profiles by considering viewing geometry, the proposed method conducts atmospheric correction at every pixel of a numerical weather prediction model in a single step calculation. The Visible Infrared Imaging Radiometer Suite (VIIRS) imaging channel (375 m) I4 (3.55–3.93  $\mu\text{m}$ ) and I5 (10.50–12.40  $\mu\text{m}$ ) bands were used as mid-wavelength and thermal infrared images to demonstrate the effectiveness of the proposed single-channel atmospheric correction method. The estimated sea surface temperatures (SSTs) obtained by the proposed method with high resolution numerical weather prediction models were compared with sea-truth temperature data from ocean buoys, multichannel-based SST products from VIIRS/MODIS, and results from MODerate resolution atmospheric TRANsmission 5 (MODTRAN 5), for validation. High resolution (1.5 km and 12 km) numerical weather prediction (NWP) models distributed by the Korea Meteorological Administration (KMA) were employed as input atmospheric data. Nighttime SST estimations with the I4 band showed a root mean squared error (RMSE) of 0.95  $^{\circ}\text{C}$ , similar to that of the VIIRS product (RMSE: 0.92  $^{\circ}\text{C}$ ) and lower than that of the MODIS product (RMSE: 1.74  $^{\circ}\text{C}$ ), while estimations with the I5 band showed an RMSE of 1.81  $^{\circ}\text{C}$ . RMSEs from MODTRAN simulations were similar (within 0.2  $^{\circ}\text{C}$ ) to those of the proposed method (I4: 0.81  $^{\circ}\text{C}$ , I5: 1.67  $^{\circ}\text{C}$ ). These results demonstrated the competitive performance of a regression-based method using high-resolution numerical weather prediction (NWP) models for atmospheric correction of single-channel infrared imaging sensors.

**Keywords:** mid-wavelength and thermal infrared; single-channel atmospheric correction; numerical weather prediction model; VIIRS; sea surface temperature

## 1. Introduction

Earth surface applications of mid-wavelength (3–5  $\mu\text{m}$ ) and thermal infrared (8–14  $\mu\text{m}$ ) (MWIR and TIR, respectively) remote sensing, including surface temperature retrieval, essentially require atmospheric correction. The commonly used methods of atmospheric correction of infrared (IR) images can be categorized as single- or multi-channel, based on the number of used spectral bands [1–5]. Currently, most land surface temperature and sea surface temperature (LST and SST, respectively) products are based on multichannel methods. The split-window (SW) algorithm is widely used for

TIR sensors, as it is easy to apply and can be used without extensive computation of radiative transfer models (RTMs) or explicit information of atmospheric conditions [1,6–9]. However, these multi-channel methods have limited application in other types of single-channel-based IR sensors, such as LANDSAT-7 [10].

Conventional single-channel atmospheric correction methods are based on radiative transfer codes or regression models; those require ancillary atmospheric data such as atmospheric profiles, total column precipitable water vapor contents (TPW), and near-surface air temperature [2,4,11–13]. Some recent studies used numerical weather prediction (NWP) models as input atmospheric information for single-channel atmospheric corrections [14–17]. However, most conventional single-channel methods calculate a single set of atmospheric correction parameters (atmospheric upwelling and downwelling radiances and transmittance) per calculation [7,18]. Depending on the radiative transfer models, the number of calculations should be increased, or even require calculations for every pixels of NWP data, in order to minimize the effects of different viewing angles, as well as atmospheric spatial inhomogeneity and to obtain a uniform atmospheric correction quality within a scene.

In this study, we provide an idea of a single-channel atmospheric correction method, with a combination of high-resolution (1.5 km and 12 km) NWP models from the Korea Meteorological Administration (KMA). By adopting a simple regression method derived from MODTRAN 5 simulations, the proposed method could calculate atmospheric correction parameters at every pixel of NWP model data with a single step calculation of the atmospheric correction process by considering target to sensor geometry.

The proposed method was applied to the VIIRS imaging channels I4 (3.55–3.93  $\mu\text{m}$ , mid-wavelength Infrared, MWIR) and I5 (10.50–12.40  $\mu\text{m}$ , thermal infrared, TIR) for sea surface temperature (SST) estimations and a performance verification of the proposed method using the SST estimation results. Both channels have spatial resolutions of 375 m and 0.4 K of on-orbit noise equivalent differential temperature (NEdT) performance [18]. VIIRS imagery was selected because it has both MWIR and TIR channels within its imaging channels, and its multi-channel-based SST product can be compared with the results of the proposed method.

The accuracy assessment was conducted by comparing the results with current SST products (from VIIRS and MODIS), SST estimation using MODTRAN 5 simulations, and sea-truth data from ocean buoys in coastal regions of the Korean Peninsula.

## 2. Materials and Methods

### 2.1. Numerical Weather Prediction Models

The Korea Meteorological Administration (KMA) has been producing NWPs with different spatial resolutions and cover areas. Two models were used in this study: Regional Data Assimilation and Prediction System (RDAPS) and Local Data Assimilation and Prediction System (LDAPS). RDAPS covers eastern Asia including Korea, Japan, China, and a part of Southeast Asia with a spatial resolution of 12 km. It analyzes atmospheric conditions four times a day (00, 06, 12, 18 UTC) and produces 30 weather predictions from +0 h to +87 h with a 3 h interval [19]. LDAPS covers the Korean Peninsula with a 1.5 km spatial resolution. Its analysis interval is 3 h (00, 03, 06, 09, 12, 15, 18, 21 UTC), and weather predictions are made at hourly intervals [19] (Figure 1). Twenty six atmospheric layers were extracted from both models: a 1.5 m geometric altitude layer and 25 isobaric layers from 1000 hpa to 50 hpa. Atmospheric temperature, pressure, relative humidity, and geopotential height were used in this study.

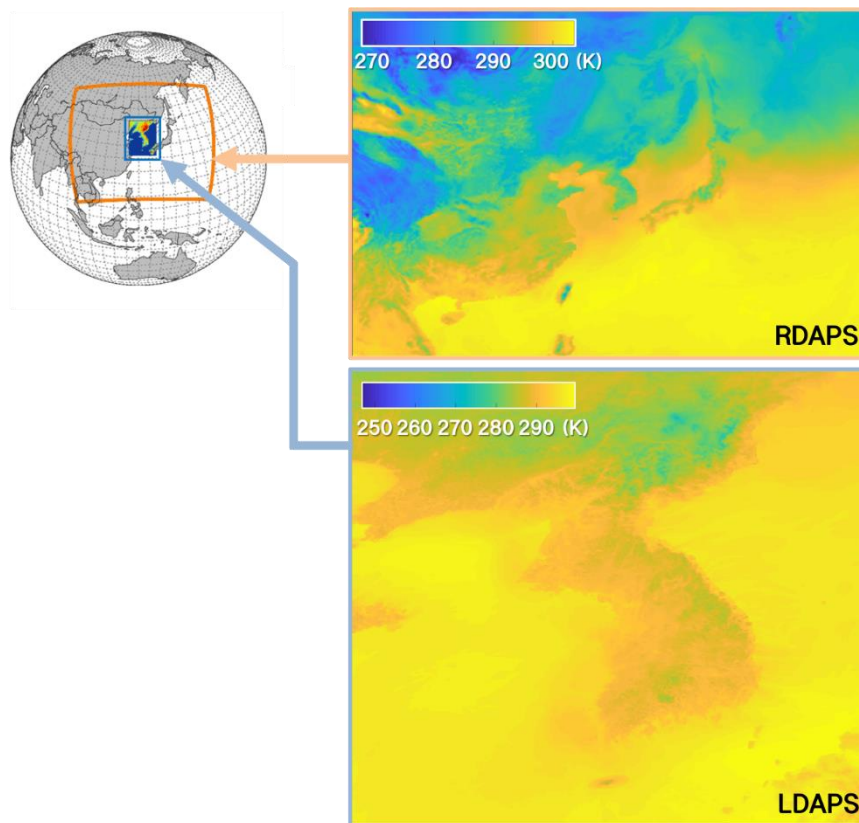


**Figure 1.** Areal coverage and examples of numerical weather prediction models of Regional Data Assimilation and Prediction System (RDAPS) and Local Data Assimilation and Prediction System (LDAPS). Examples of atmospheric temperatures at 1.5 m geometric altitude layers, analyzed 4 September 2014, 18:00 UTC and +0 h prediction. The data and coverage map were obtained from the Korea Meteorological Administration (KMA) National Meteorological Super Computer Center [19].

## 2.2. Formulation of a Regression Model

To maintain simplicity, the single-channel atmospheric correction algorithm proposed in this study was based on the following basic atmospheric radiative transfer equations [20,21]:

$$I_{\lambda, \uparrow, \text{at TOA}}^{\text{atm}} = \int_0^{\tau_{\text{surf}}} B_{\lambda}(T_{\tau'}) e^{-(\tau'-0)/\mu} \frac{d\tau'}{\mu} \quad (1)$$

$$I_{\lambda, \downarrow, \text{at Surf}}^{\text{atm}} = \int_0^{\tau_{\text{surf}}} B_{\lambda}(T_{\tau'}) e^{-(\tau_{\text{surf}}-\tau')/\mu} \frac{d\tau'}{\mu} \quad (2)$$

$$T_{\lambda} = \exp(-\tau_{\text{surf}}/\mu) \quad (3)$$

where  $I_{\lambda, \uparrow, \text{at TOA}}^{\text{atm}}$  is the spectral atmospheric upwelling radiance measured at the top of the atmosphere (TOA) and  $I_{\lambda, \downarrow, \text{at Surf}}^{\text{atm}}$  is the spectral atmospheric downwelling radiance measured at the Earth's surface. Both atmospheric radiances can be calculated by integrations from optical thickness of TOA level ( $\tau_{\text{TOA}} = 0$ ) to that of the Earth's surface ( $\tau_{\text{surf}}$ ), with a consideration of light path geometry ( $\mu$ , cosine of path zenith angle).

$B_{\lambda}$  is Planck's function acting as a source function under the local thermal equilibrium condition.  $T_{\lambda}$  is the spectral atmospheric transmittance for a total radiation path from the surface to the TOA. Unlike other variables in Equations (1) to (3), optical thickness can neither be easily acquired from NWP data, nor simply calculated. Therefore, a regression model was formulated for calculating

the optical thickness. Under clear-sky conditions with low aerosol content, the scattering process of atmospheric molecules in the 3–15  $\mu\text{m}$  infrared region is not as significant as that in shorter wavelength regions [20–23]. For satellite remote sensing applications upon the Earth's surface with clear-sky conditions, those exclude cloud/fog/aerosol contaminated images. Therefore, to maintain simplicity, the regression model was focused only on an absorption process in this study.

An optical thickness between altitudes  $z_0$  and  $z_1$  could be calculated by Equation (4), without considering the scattering process.

$$\tau_\lambda(z_0, z_1) = \int_{z_0}^{z_1} k_\lambda^{abs} \rho_{abs} dz \quad (4)$$

Here,  $k_\lambda^{abs}$  is an absorption coefficient for wavelength  $\lambda$ , and  $\rho_{abs}$  is the density of atmospheric molecules that contribute to the absorption process. With multiple gas species, an absorption coefficient can be expressed as a summation of the  $i^{th}$  absorption lines of the  $n^{th}$  gas species for the center wavelength  $\lambda$  with the strength function  $S_i(T)$  and the line shape function  $f_{i,\lambda}(p, T)$ , given by Equation (5) [20,22].

$$k_\lambda^{abs} = \sum_{n=1}^N \sum_{i=1}^I S_{n,i}(T) f_{\lambda,n,i}(p, T) \quad (5)$$

Since Equation (5) is a simple summation, the absorption coefficient can be separated into terms of dry air,  $k_{\lambda,dry}^{abs}$ , and water vapor,  $k_{\lambda,wv}^{abs}$ :

$$k_\lambda^{abs} = \sum_{n=1}^{N-1} \sum_{i=1}^I S_{n,i}(T) f_{\lambda,n,i}(p, T) + \sum_{i=1}^I S_{wv,i}(T) f_{\lambda,wv,i}(p, T) = k_{\lambda,dry}^{abs} + k_{\lambda,wv}^{abs} \quad (6)$$

Dividing the absorption coefficients and pre-calculating coefficients according to infrared sensors have been attempted in previous studies [24]. In this study, however, an exponential function was employed to increase the simplicity of the regression model and minimize pre-calculation while utilizing NWP models and obtaining 3D atmospheric information from the models [20].

$$k_\lambda^{abs} \approx k_\lambda^{abs}(p_{ref}, T_{ref}) \left( \frac{p}{p_{ref}} \right)^{np} \left( \frac{T_{ref}}{T} \right)^{nT} \quad (7)$$

Here, an absorption coefficient can be expressed as a function of atmospheric pressure,  $p$ , and temperature,  $T$ .  $k_\lambda^{abs}(p_{ref}, T_{ref})$  is the coefficient acquired under reference conditions with pressure,  $p_{ref}$ , and temperature,  $T_{ref}$ .  $np$  and  $nT$  are exponential terms for pressure and temperature, respectively. Therefore, the atmospheric absorption introduced in Equation (5) can be expressed as Equation (8), by combining Equations (6) and (7).

$$\begin{aligned} k_\lambda^{abs} &= k_{\lambda,dry}^{abs} + k_{\lambda,wv}^{abs} \\ &\approx k_{\lambda,dry}^{abs}(p_{ref}, T_{ref}) \left( \frac{p}{p_{ref}} \right)^{np} \left( \frac{T_{ref}}{T} \right)^{nT} \\ &\quad + k_{\lambda,wv}^{abs}(p_{ref}, T_{ref}) \left( \frac{p}{p_{ref}} \right)^{np} \left( \frac{T_{ref}}{T} \right)^{nT} \end{aligned} \quad (8)$$

The optical thickness can then be calculated with integrations of exponential functions by substituting Equation (8) into Equation (4).

$$\begin{aligned}
 \tau_\lambda(z_0, z_1) &= \int_{z_0}^{z_1} k_\lambda^{abs} \rho_{abs} dz = \int_{z_0}^{z_1} \left( k_{\lambda, dry}^{abs} \rho_{dry} + k_{\lambda, wv}^{abs} \rho_{wv} \right) dz \\
 &= k_{(\lambda, dry)}^{abs} (p_{ref}, T_{ref}) \int_{z_0}^{z_1} \left( \left( \frac{p_z}{p_{ref}} \right)^{np} \left( \frac{T_{ref}}{T_z} \right)^{nT} \rho_z, dry \right) dz \\
 &\quad + k_{(\lambda, wv)}^{abs} (p_{ref}, T_{ref}) \int_{z_0}^{z_1} \left( \left( \frac{p_z}{p_{ref}} \right)^{np} \left( \frac{T_{ref}}{T_z} \right)^{nT} \rho_z, wv \right) dz
 \end{aligned}
 \tag{9}$$

The integrations in Equation (9) can be solved through a multivariate regression analysis, in which the two integration terms are considered as two independent variables ( $x, y$ ), and the dry air and water vapor reference absorption coefficients  $k_{\lambda, dry}^{abs}(p_{ref}, T_{ref})$  and  $k_{\lambda, wv}^{abs}(p_{ref}, T_{ref})$  were used as the regression coefficients ( $P_1, P_2$ , respectively).

$$\tau_\lambda(z_0, z_1) \equiv P_1 x + P_2 y \tag{10}$$

Since the reference absorption coefficients become regression coefficients, arbitrary values of  $p_{ref}$  and  $T_{ref}$  can be used. These values were set as 1013 hpa and 290 K, respectively, following typical ambient atmospheric pressure and temperature conditions. Instead of the 1st order polynomial regression model of Equation (10), a 3rd order polynomial is practically a more realistic regression model, as given by Equation (11).

$$\tau_\lambda(z_0, z_1) \equiv P_0 + P_1 x + P_2 y + P_3 x^2 + P_4 xy + P_5 y^2 + P_6 x^3 + P_7 x^2 y + P_8 xy^2 + P_9 y^3 \tag{11}$$

In the proposed 3rd order polynomials, the strict physical meanings of the regression coefficients as the reference absorption coefficients are loosened. However, the 3rd order polynomials are generally a better fit to the actual atmospheric conditions as compared to the 1st order polynomials. Thus, Equation (11) was adopted in this study instead of Equation (10) in order to provide atmospheric optical thickness values and the solution for Equations (1) to (3).

### 2.3. Determination of Model Parameters

A normal equation was employed to determine regression parameters.

$$\begin{aligned}
 \theta &= (X^T X)^{-1} X^T \hat{\tau} \\
 \text{where, } \hat{\tau} &= \left[ \tau_{1,\lambda, total} \quad \tau_{2,\lambda, total} \quad \dots \quad \tau_{n,\lambda, total} \right]^T \\
 X &= \begin{bmatrix} 1 & x_1 & y_1 & x_1^2 & x_1 y_1 & y_1^2 & x_1^3 & x_1^2 y_1 & x_1 y_1^2 & y_1^3 \\ 1 & x_2 & y_2 & x_2^2 & x_2 y_2 & y_2^2 & x_2^3 & x_2^2 y_2 & x_2 y_2^2 & y_2^3 \\ \vdots & \vdots \\ 1 & x_n & y_n & x_n^2 & x_n y_n & y_n^2 & x_n^3 & x_n^2 y_n & x_n y_n^2 & y_n^3 \end{bmatrix} \\
 \theta &= [P_1 \quad P_2 \quad P_3 \quad P_4 \quad P_5 \quad P_6 \quad P_7 \quad P_8 \quad P_9]^T
 \end{aligned}
 \tag{12}$$

An observation vector,  $\hat{\tau}$ , is the optical thickness obtained during the MODTRAN 5 simulation, and the variables  $x_n, y_n$  are calculated from the  $n^{th}$  atmospheric profile used for the simulation (Figure 2). A total of 520 MODTRAN simulations were conducted to gain values for an observation vector. A total of 26 atmospheric columns were used, with two profiles per month and one extra profile for August and January. A total of 20 sensor altitude settings were applied to the atmospheric profiles, from 0 km to 19 km with an interval of one kilometer.

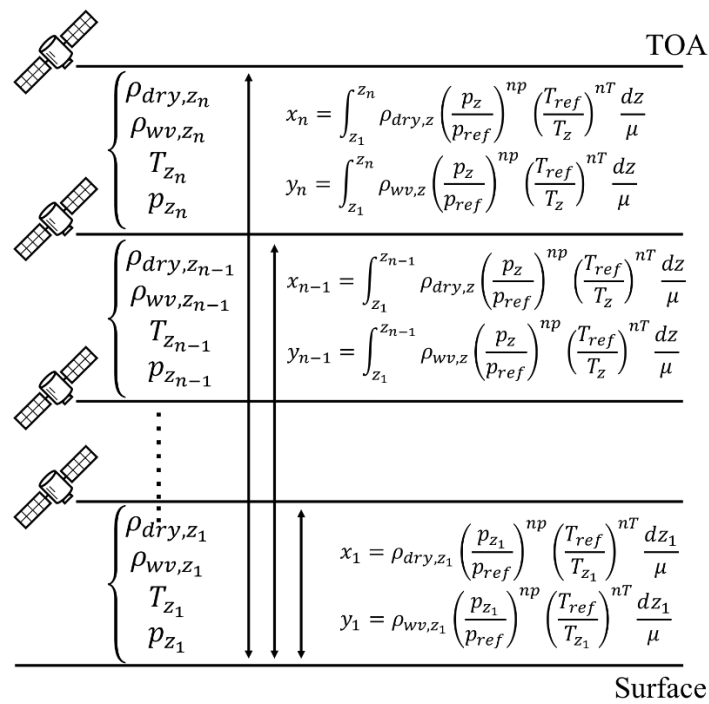


**Figure 2.** A schematic diagram for the simulation of atmospheric layers with multiple sensor altitudes and conditions.

After the calculation of regression coefficients, the least-squares of  $\hat{\tau}'$  can easily be obtained by:

$$\hat{\tau}' = X\theta \tag{13}$$

Regression analysis, using Equations (12) and (13), was conducted with various combinations of exponent terms  $np$  and  $nT$  from Equations (7) and (8). The combination that resulted in the best fit model was used for the final calculation of the coefficient  $P_n$ . Figure 3 shows the distributions of RMSEs calculated from the observation vector and least-squares fitted values according to the combinations of the exponent terms and minimum RMSEs.

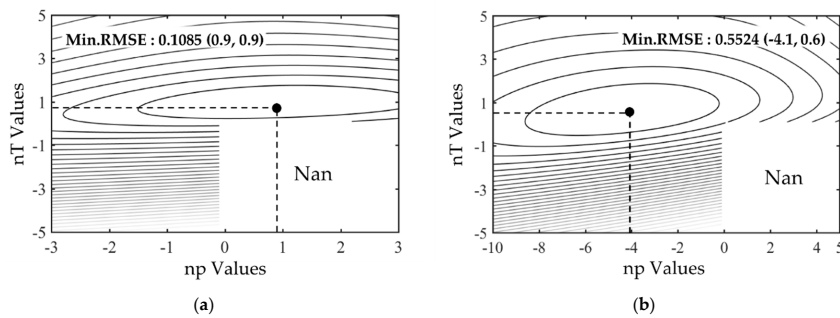


**Figure 3.** Cont.

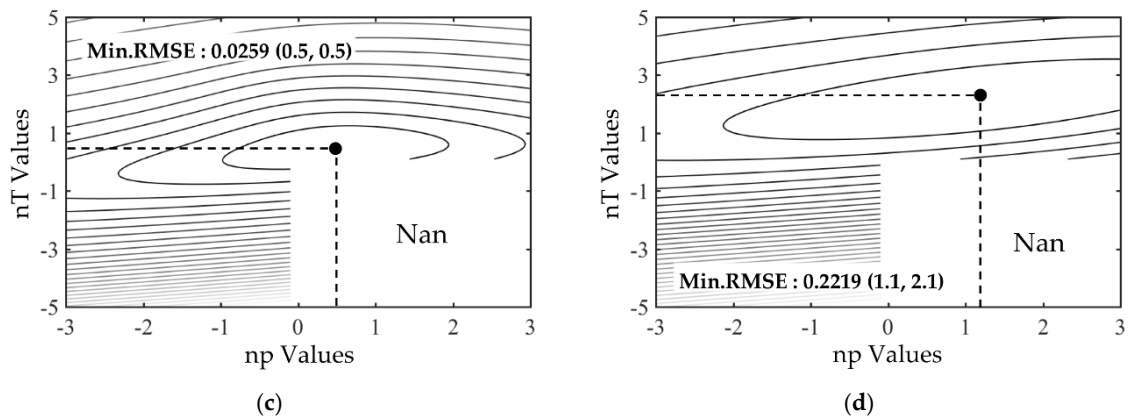


**Figure 3.** Distributions of RMSEs calculated from the observation vector and fitted values according to various combinations of exponent terms used for the regression analysis: (a) 1st order regression for the VIIRS I4 band (MWIR) and (b) 1st order regression for the VIIRS I5 band (TIR); (c) 3rd order regression for the VIIRS I4 band (MWIR) and (d) 3rd order regression for the VIIRS I5 band (TIR). The suggested values of  $np$  and  $nT$  were 1 and 0.5, respectively [20]. However, Figure 3 implies that the best fit results were obtained at a point different from (1, 0.5). Additionally, the minimum RMSEs of the 3rd order polynomial regressions were smaller than those of the 1st order polynomial regression, suggesting that the fits of the former are better. The optimal regression coefficients obtained in this study for infrared satellite systems are summarized in Table 1.

**Table 1.** Regression coefficients used for the infrared satellite systems.

System	$P_0$ $P_5$	$P_1$ $P_6$	$P_2$ $P_7$	$P_3$ $P_8$	$P_4$ $P_9$
<b>VIIRS I4 (MWIR)</b>	0.00148 0.00000912	0.795 0.409	0.000499 −0.000928	−0.528 0.0000285	−0.00294 −0.0000000671
<b>VIIRS I5 (TIR)</b>	0.0318 0.000147	2.78 −4.43	−0.00497 −0.00511	4.79 0.000497	−0.0585 −0.00000116

#### 2.4. Corrections of Model Biases

By applying the proposed regression model for the optical thickness (Equation (11), Table 1) and radiative transfer equations (Equations (1) to (3)), preliminary calculations of the atmospheric correction parameters via the radiative transfer equations were conducted. Figures 4 and 5 display comparisons between the preliminary calculation results and simulation results from MODTRAN 5, under a nadir observation condition. Comparisons before and after model bias corrections under a nadir observation condition are both provided in the following Figures 4 and 5.

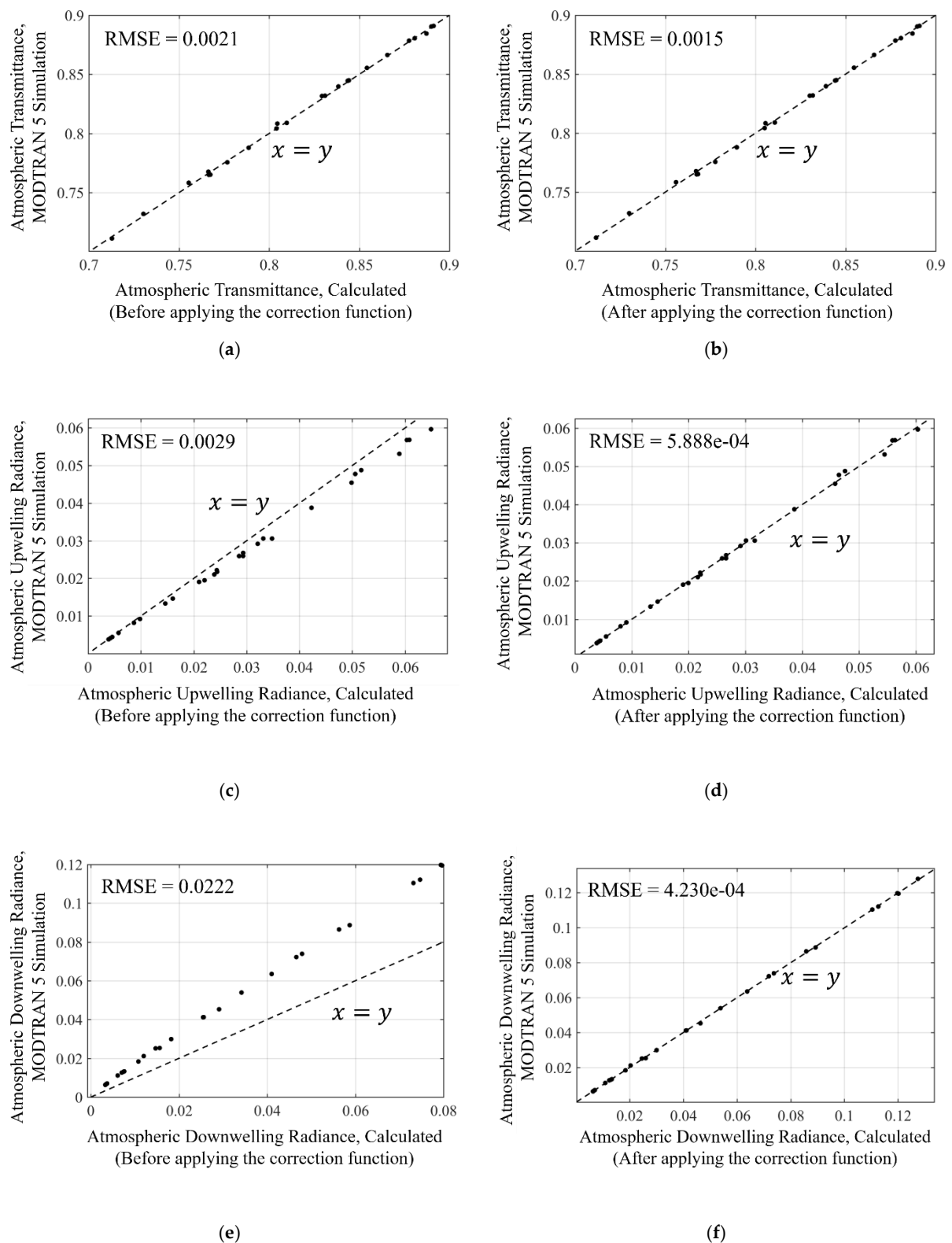
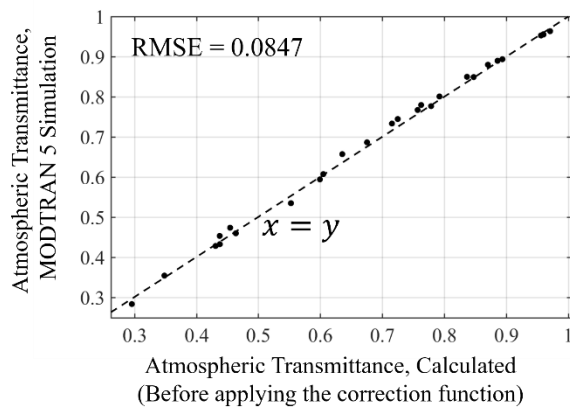
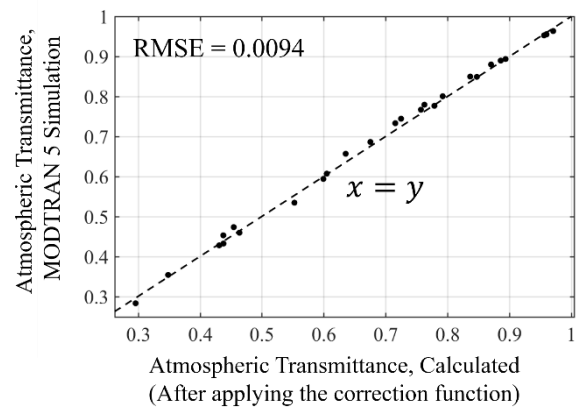


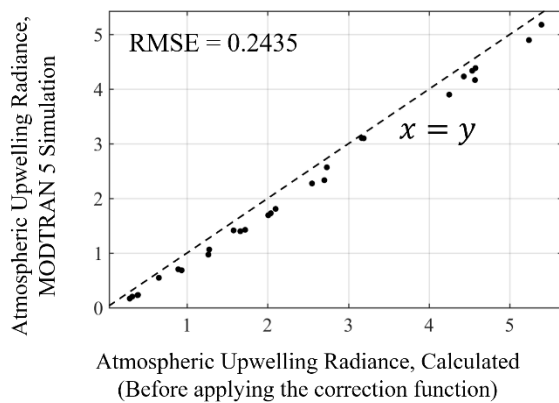
**Figure 4.** Comparison of the atmospheric correction parameters between the results calculated from the proposed regression model with radiative transfer equations and simulation results from MODTRAN 5, under a nadir observation condition (VIIRS I4 band): (a,c,e) before correcting for model biases; (b,d,f) after correcting for model biases.



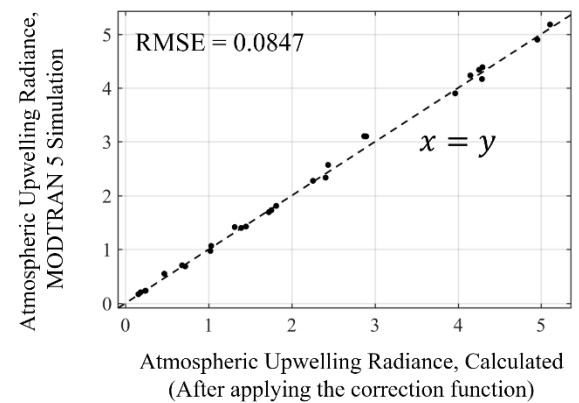
(a)



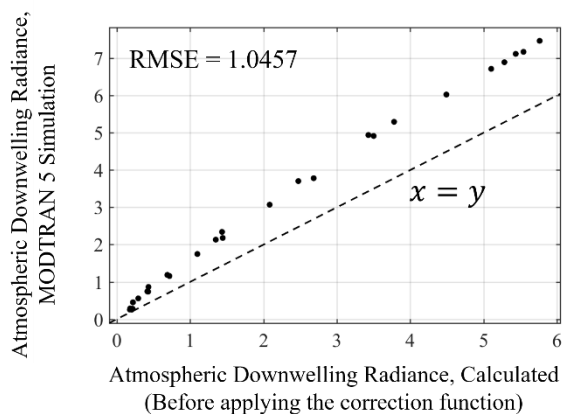
(b)



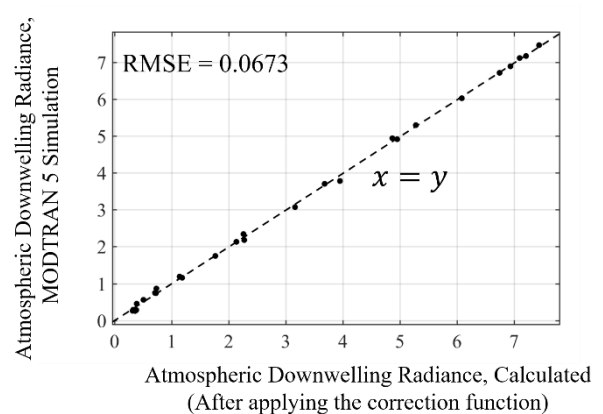
(c)



(d)



(e)



(f)

**Figure 5.** Comparison of the atmospheric correction parameters between the results calculated from the proposed regression model with radiative transfer equations and simulation results from MODTRAN 5, under nadir observation conditions: (a,c,e) before correcting for model biases; (b,d,f) after correcting for model biases.

The model biases could be corrected by matching preliminary calculation results to the MODTRAN 5 simulated results, with a polynomial regression. Model bias correction functions for VIIRS I4 and I5 bands are listed in Equations (14) to (16). As seen in Figures 4 and 5, the model bias of atmospheric downwelling radiances was significant for both VIIRS I4 and I5 bands, while that of the atmospheric transmittance values was relatively insignificant. The atmospheric transmittance could be directly calculated from optical thickness values with the proposed regression model in Equation (11). On the other hand, only path radiance and extinction were considered in the calculation of atmospheric radiances. Therefore, ground/near-ground multiple scattering could contribute to the model biases when calculating downwelling radiance between the proposed model and the MODTRAN. In order to simplify this process, the effects of the ground/near ground multiple scattering were treated as model bias and corrected with regression models (Figures 4e and 5e).

$$T_{\lambda}(x) = \begin{cases} 0.9875x^3 - 2.595x^2 + 3.255x - 0.6478 & (I4 \text{ band, MWIR}) \\ -1.187x^4 + 2.852x^3 - 2.572x^2 + 2.045x - 0.1528 & (I5 \text{ band, LWIR}) \\ \text{where, } x = T_{\lambda} \text{ from radiative transfer equations} \end{cases} \quad (14)$$

$$I_{(\lambda, \uparrow, \text{at TOA})}^{\text{atm}}(x) = \begin{cases} n(0.4563x^3 + 0.8519x^2 + 0.865x - 0.0005) & (I4 \text{ band, MWIR}) \\ -0.004x^3 + 0.0499x^2 + 0.820x - 0.0877 & (I5 \text{ band, LWIR}) \\ \text{where, } x = I_{(\lambda, \uparrow, \text{at TOA})}^{\text{atm}} \text{ from radiative transfer equations.} \end{cases} \quad (15)$$

$$I_{(\lambda, \downarrow, \text{at Surf})}^{\text{atm}}(x) = \begin{cases} n(30.45x^3 + 4.615x^2 + 1.67x - 0.001) & (I4 \text{ band, MWIR}) \\ -0.004x^3 + 0.0949x^2 + 1.686x - 0.0198 & (I5 \text{ band, LWIR}) \\ \text{where, } x = I_{(\lambda, \downarrow, \text{at Surf})}^{\text{atm}} \text{ from radiative transfer equations.} \end{cases} \quad (16)$$

As shown in Figures 4b and 5b, the RMSEs were significantly reduced after the model bias correction. Figure 6 shows examples of calculated atmospheric downwelling radiances after correcting for the model bias, compared to MODTRAN 5 simulation results under various observation angles. The two results were linearly correlated without any offsets, implying that model biases were successfully separated from the effects of observation angles. Correction functions for these effects are listed in Equations (17) to (19).

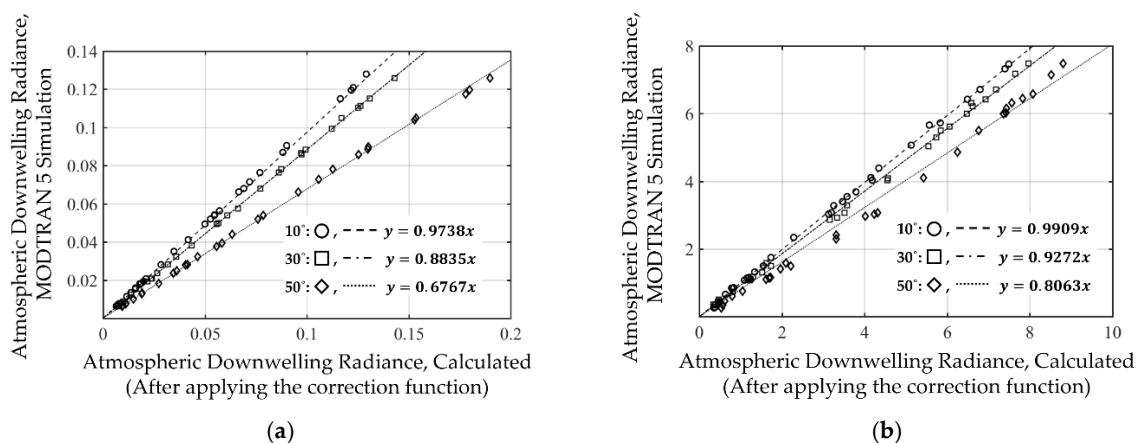


**Figure 6.** Comparison of the atmospheric downwelling radiances ( $W/m^2/sr/\mu m$ ) between the proposed regression model after the model bias correction and the simulated results of MODTRAN 5, under various observation angles: (a) for the VIIRS I4 band; (b) for the VIIRS I5 band.

$$A_{\lambda, Trans}(\theta) = \begin{cases} 1.001 \sin \{0.07362 \tan (1.35\theta) + 1.574\} & (I4 \text{ band, MWIR}) \\ \sin \{0.1415 \tan (1.25\theta) + 1.558\} & (I5 \text{ band, LWIR}) \\ \text{where, } \theta \text{ in degree} \end{cases} \quad (17)$$

$$A_{\lambda,up}(\theta) = \begin{cases} 1/\{1.005 \sin(0.09463 \tan(1.35\theta) + 1.498)\} & \text{(I4 band, MWIR)} \\ 1/\{1.002 \sin\{0.1898 \tan(1.15\theta) + 1.553\}\} & \text{(I5 band, LWIR)} \\ \text{where, } \theta \text{ in degree} \end{cases} \quad (18)$$

$$A_{\lambda,dwr}(\theta) = \begin{cases} 0.9994 \sin\{0.0172\theta + 1.538\} & \text{(I4 band, MWIR)} \\ 1.001 \sin\{0.1257\theta + 1.58\} & \text{(I5 band, LWIR)} \\ \text{where, } \theta \text{ in degree} \end{cases} \quad (19)$$

where  $\theta$  is the observation zenith angle.

The effects from observation angles can be corrected by multiplying slopes according to observation angles. An example of acquiring atmospheric transmittance is shown below (Equation (20)), where  $T_{\lambda, \text{final}}(x, \theta)$  is a result after two steps of correction functions.

$$T_{\lambda, \text{final}}(x, \theta) = A_{\lambda, \text{Trans}}(\theta) \times T_{\lambda}(x) \quad (20)$$

### 2.5. Processing Steps

Processing of the proposed single-channel atmospheric correction method consisted of four steps: stacking atmospheric layers into 3D cubes, interpolating the layers, re-organizing atmospheric blocks according to the observation geometry, and calculating atmospheric correction parameters (Figure 7).

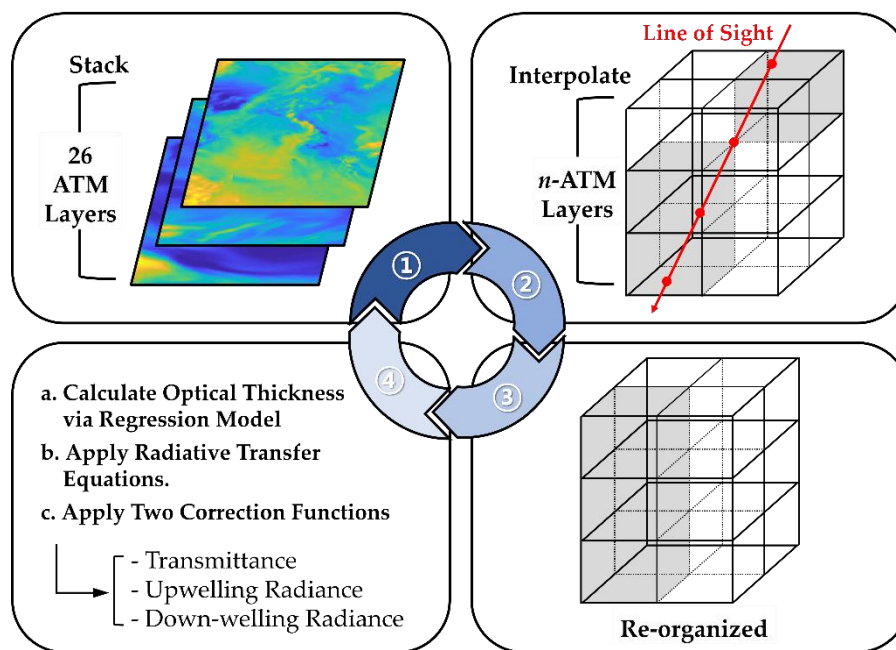


**Figure 7.** Schematic diagram depicting the proposed single-channel atmospheric correction method, which consists of four steps, including the atmospheric blocks re-organization procedure to accommodate various observation angles.

First, model surfaces and isobaric surfaces from numerical weather prediction models were stacked according to their geometric altitudes. The models provided geopotential altitudes. Therefore, the altitudes were converted as per the following equation [25]:

$$Z = \frac{EH}{E - H} \text{ (Units : m)} \quad (21)$$

where  $Z$  is the geometric altitude,  $H$  is the geopotential altitude, and  $E$  is the radius of the Earth. The radius was set as 6,371,229 m, following the value assigned by the KMA in the numerical models. In total, four datasets were stacked: temperature, relative humidity, pressure, and altitude.

After the altitude unit conversion, the geometric altitudes of each dataset were different. To conduct re-organization in Step 3 and to conduct integration in Equations (1) and (2), every dataset must be in a unified altitude system through an interpolation. Figure 8 shows the variation of average errors from SST estimations according to the numbers of the interpolated atmospheric layers. In the figure, as the number of interpolations increases, the average error of the MWIR region decreases. Even though the decrease after 300 layers was insignificant, atmospheric datasets were interpolated to 2000 layers for the MWIR region to obtain the best accuracy. For the TIR region, however, the minimum average error occurred near 300 layers, and therefore, the datasets were interpolated up to 300 layers.

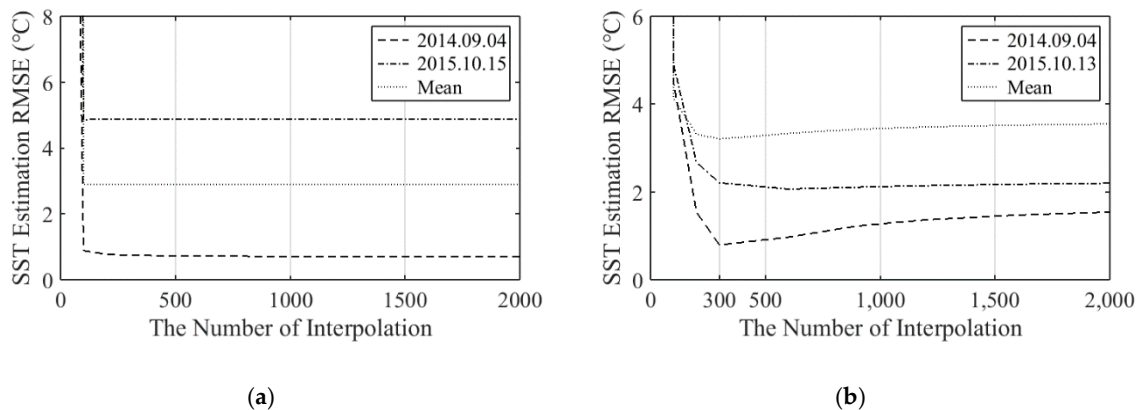


**Figure 8.** Error patterns of SST estimations according to the numbers of atmospheric layer interpolations: (a) absolute values of average errors of SST estimation with VIIRS I4 band (MWIR); (b) absolute values of average errors of SST estimation with VIIRS I5 band (TIR).

After the datasets were interpolated, re-organization was conducted for each pixel within a scene, considering the observation geometry of the sensor. Infrared images were assumed to have a row-column coordinate system with a north-up orientation that started from the top-left corner. Each pixel on the lowest atmospheric layer was considered as an individual starting point, with row and column coordinates of  $r_0$  and  $c_0$ , respectively. The following equations were then applied to re-organize the atmospheric dataset.

$$r_n = \left[ \sum_{i=1}^{n-1} -\{ \tan(\theta) \sin(\varphi) \} dz_i / dx \right] + r_0 \quad (22)$$

$$c_n = \left[ \sum_{i=1}^{n-1} -\{ \tan(\theta) \cos(\varphi) \} dz_i / dx \right] + c_0 \quad (23)$$

where  $\theta$  and  $\varphi$  are the satellite zenith angle and azimuth angle, respectively, and  $dz_i$  is the thickness of the  $i^{th}$  atmospheric layer. The result,  $(r_n, c_n)$ , indicated row-column coordinates of pixels on the  $n$ th layer and that its value would be relocated to  $(r_0, c_0, n)$ . The re-organization process was essential for the proposed algorithm to accommodate various satellite observations and increase its compatibility. By conducting the re-organization, calculation over a whole ROI in a vertical direction with a single process became possible, while considering sensor-viewing geometry.

The optical thickness of each atmospheric layers was calculated with the developed regression model with Equation (11) and the coefficients introduced in Table 1. The calculated atmospheric thickness was used to acquire the three atmospheric correction parameters (atmospheric up-/down-welling radiances and transmittance) from radiative transfer equations (Equations (1) to (3)), along with atmospheric temperature information from atmospheric profiles. Two-step correction functions were applied to remove the model biases of the results.

### 3. Results and Validations

#### 3.1. Atmospheric Correction Parameters

The calculated values of atmospheric correction parameters were compared with the simulated results from MODTRAN 5. The RMSEs according to observation angles are summarized in Table 2. The parameters were calculated for VIIRS imaging channels I4 and I5 by the single-channel method proposed in this study. A total of 24 RDAPS data were randomly selected, and atmospheric profiles from 28 reference points (Figure 9 and Table 3) were also extracted from each RDAPS data.

The atmospheric transmittance values with an observation angle of 50 degrees ranged between 0.55–0.9 and 0.2–0.9 for the VIIRS I4 and I5 bands, respectively. The RMSEs of the transmittances from the proposed method showed 0.6% (I4 band) and 8% (I5 band) of their minimum values with the same observation angle. Under an observation angle of 60 degrees, error levels increased to 2.8% (0.4–0.77, I4 band) and 60% (0.1–0.8, I5 band) of the minimum transmittance values.

Atmospheric upwelling (I4: 0.005–0.1 and I5: 0.4–6.8 W/m<sup>2</sup>/sr/μm) and downwelling (I4: 0.07–0.125, I5: 0.4–7.1 W/m<sup>2</sup>/sr/μm) radiances for VIIRS imaging channels had RMSE values less than 2–3% of their maximum values with an observation angle of 50 degrees. The RMSE levels increased by up to 60% as compared to their minimum radiance magnitudes. After the angle was increased to 60 degrees, the RMSEs of upwelling (I4: 0.005–0.14, I5: 0.5–7.5 W/m<sup>2</sup>/sr/μm) and downwelling (I4: 0.005–0.13, I5: 0.4–6.9 W/m<sup>2</sup>/sr/μm) radiances were less than 4% of the maximum values and less than 60% of the minimum values.

**Table 2.** RMSEs of atmospheric correction parameters as compared to MODTRAN 5.

Systems and Observation Angles		0°	10°	20°	30°	40°	50°	60°
I4 band	$I_{\lambda, \uparrow, at TOA}^{atm}$	0.000589	0.000381	0.000429	0.000493	0.000820	0.0014	0.0032
	$I_{\lambda, \downarrow, at surf}^{atm}$	0.000423	0.000410	0.000560	0.000463	0.000759	0.0011	0.0021
	$\tau_{\lambda, \uparrow}$	0.0015	0.0012	0.0016	0.0014	0.0033	0.0032	0.011
I5 band	$I_{\lambda, \uparrow, at TOA}^{atm}$	0.0863	0.0632	0.0527	0.0599	0.0822	0.0720	0.262
	$I_{\lambda, \downarrow, at surf}^{atm}$	0.0680	0.0604	0.0935	0.0924	0.148	0.216	0.267
	$\tau_{\lambda, \uparrow}$	0.00940	0.00710	0.00660	0.00700	0.0128	0.0171	0.0616

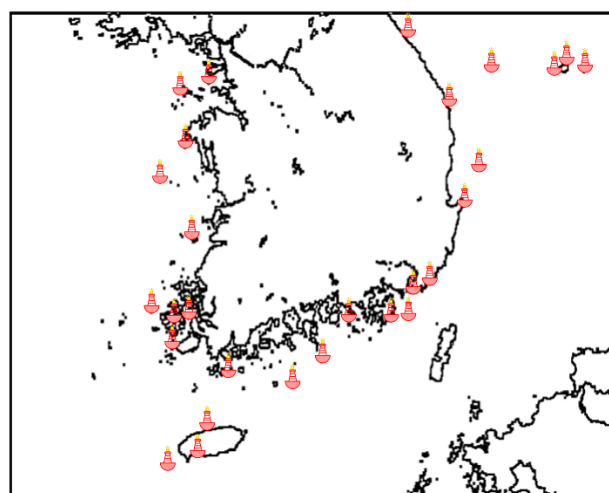


**Figure 9.** Distribution of ocean buoys around the southern part of Korean Peninsula, providing sea-truth temperature data for validation.

**Table 3.** A list of ocean buoys providing sea-truth temperature data for validation.

Locations of Ocean Buoys Employed for Validation					
No.	Location	Coordinates	No.	Location	Coordinates
1	Deokjeok-Do (isl. *)	37°14'10"N/126°01'08"E	15	Cheongsan-Do (isl.)	34°08'17"N/126°44'39"E
2	Oeyeon-Do (isl.)	36°15'00"N/125°45'00"E	16	Geoje-Do (isl.)	34°46'00"N/128°54'00"E
3	Seosu-Do (isl.)	37°19'30"N/126°23'36"E	17	Haeundae	35°08'56"N/129°10'11"E
4	Sinjin-Do (isl.)	36°36'18"N/126°07'34"E	18	Dumi-Do (isl.)	34°44'40"N/128°10'30"E
5	Chilbal-Do (isl.)	34°47'36"N/125°46'37"E	19	Haegumgang	34°44'09"N/128°41'27"E
6	Chinan	34°44'00"N/126°14'30"E	20	Busan Harbor	35°01'21"N/128°57'22"E
7	Galmaeyeo	35°36'48"N/126°14'42"E	21	Pohang	36°21'00"N/129°47'00"E
8	Ock-Do (isl.)	34°41'34" N/126°03'20"E	22	Jukbyeon	37°06'15" N/129°23'22"E
9	Jin-Do (isl.)	34°26'33" N/126°03'25"E	23	Guryongpo	35°59'52" N/129°35'10"E
10	Mara-Do (isl.)	33°05'00" N/126°02'00"E	24	Ulleung-Do (isl.)	37°27'20"N/131°06'52"E
11	Jeju Harbor	33°31'31"N/126°29'38"E	25	Donghae	37°28'50"N/129°57'00"E
12	Joong Moon	33°13'31"N/126°23'35"E	26	Hyeolam	37°32'29"N/130°51'15"E
13	Geomun-Do (isl.)	34°00'05"N/127°30'05"E	27	Goo-am	37°28'44"N/130°48'16"E
14	Ganyeoam	34°17'06"N/127°51'28"E	28	Yeongok	37°52'03"N/128°53'08"E

\* isl.: Island

### 3.2. Accuracy of Sea Surface Temperature Estimations

The proposed single-channel atmospheric correction method was applied to estimate SST to validate its accuracy. Sea surface emissivity values were calculated using a simple model and the ASTER spectral library [26,27]. The estimated SST values were compared with sea-truth temperature data gathered from 28 buoys, scattered around the southern part of the Korean Peninsula (Figure 9 and Table 3). Those buoys corresponded to the prediction area of the KMA NWP models (Figure 1) [28].

Three types of remotely sensed SSTs were compared to sea-truth temperatures obtained from ocean buoys (Figure 10 and Table 4), which included SSTs computed by the proposed method, a single-channel method using MODTRAN 5 simulations for every validation point, and SST products of VIIRS/MODIS (VIIRS SST Product: VIIRS\_NPP-OSPO-L2P-v2.4, MODIS SST Product: MODIS\_A-JPL-L2P-v2014.0) [29,30]. SST estimations using MODTRAN5 were conducted using atmospheric profiles extracted after the re-organization process described in Section 2.5, for comparing the results under similar conditions.

At night, in the absence of the solar signal, all four errors of the I4 band (mean, Std., Max., RMSE) were larger while using the proposed single-channel method than while using the MODTRAN on the VIIRS I4 band (Table 4). However, their differences were less than 0.2 °C. RMSE, and the standard deviation of the I4 band, based on the proposed method, was similar to that of the VIIRS SST product and half of the MODIS SST product. The maximum absolute error from the proposed method applied to the I4 band was smaller than that of the VIIRS product. The values obtained for the I4 band using the proposed method were biased by −0.39 °C, as shown in Table 4.

For the I5 band, the proposed method showed the largest RMSE and standard deviation among the four different SSTs. However, the mean error and maximum absolute error were the smallest at −0.07 °C and 6.39 °C, respectively. During the daytime, a mean error of the proposed method using the I5 band was slightly more than the VIIRS and MODIS SST products. Additionally, standard deviations of nighttime results showed the MODIS product and the I5 band results with broader error distributions and larger standard deviations. The VIIRS product and I4 band, which had more concentrated distributions, showed smaller standard deviations.

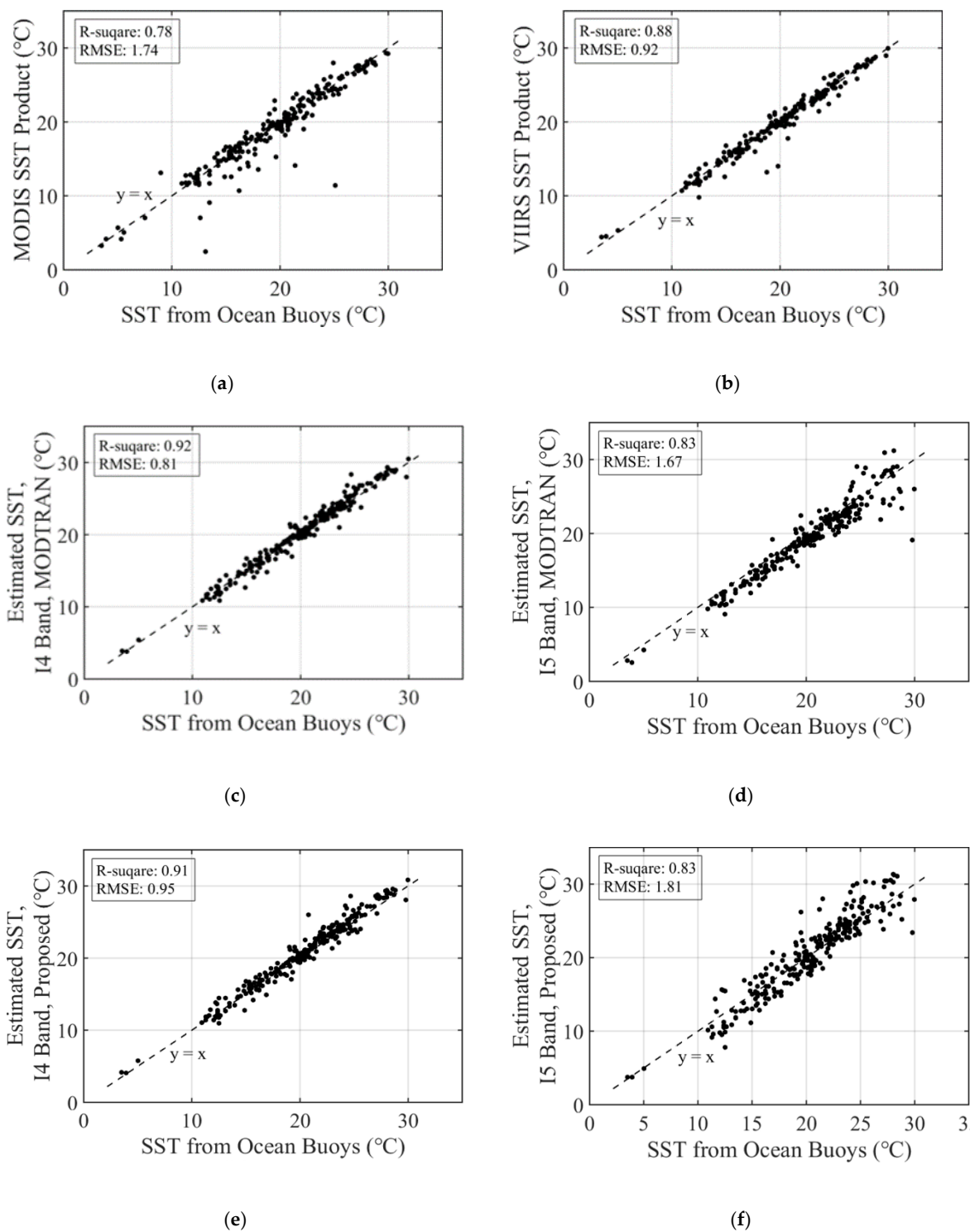


**Figure 10.** Nighttime sea surface temperature from ocean buoys versus the SST measure by the MODTRAN 5, proposed method, and existing SST products. (a) MODIS SST product (MODIS\_A-JPL-L2P-v2014.0) [30], (b) VIIRS SST product (VIIRS\_NPP-OSPO-L2P-v2.4) [29], (c) VIIRS I4 band processed by MODTRAN, (d) VIIRS I5 band processed by MODTRAN, (e) VIIRS I4 band processed by the proposed method, and (f) VIIRS I5 band processed by the proposed method.

**Table 4.** Analysis of the estimated SST as derived from VIIRS imaging channels with the proposed single-channel atmospheric correction method, compared with the SST products of VIIRS and MODIS based on multichannel atmospheric correction methods.

Time	SST Data	Samples		Errors ( °C)		
Night	Estimated SST, I4 Band, Proposed	258	Mean	−0.39	RMSE	0.95
			Std.	0.86	Max. (abs)	3.86
	Estimated SST, I5 Band, Proposed	258	Mean	−0.07	RMSE	1.81
			Std.	1.80	Max. (abs)	6.39
	Estimated SST, I4 Band, MODTRAN	258	Mean	−0.23	RMSE	0.81
			Std.	0.78	Max. (abs)	3.66
	Estimated SST, I5 Band, MODTRAN	258	Mean	0.91	RMSE	1.67
			Std.	1.40	Max. (abs)	10.7
	VIIRS SST Product *	210	Mean	0.06	RMSE	0.92
			Std.	0.91	Max. (abs)	5.75
MODIS SST Product **	215	Mean	0.33	RMSE	1.74	
		Std.	1.75	Max. (abs)	13.6	
Day	Estimated SST, I5 Band, Proposed	240	Mean	−0.37	RMSE	1.95
			Std.	1.91	Max. (abs)	6.14
	VIIRS SST Product *	179	Mean	−0.14	RMSE	1.95
			Std.	1.94	Max. (abs)	13.5
	MODIS SST Product **	219	Mean	−0.02	RMSE	2.62
			Std.	2.62	Max. (abs)	14.3

\* VIIRS SST Product: VIIRS\_NPP-OSPO-L2P-v2.4 [29]; \*\* MODIS SST Product: MODIS\_A-JPL-L2P-v2014.0 [30].

## 4. Discussions

### 4.1. Model Validations

Even though RMSEs compared to the minimum values of the atmospheric correction parameters were up to 60%, the comparison results in Table 2 suggested that the simplified regression models were successfully able to provide the parameters with an accuracy comparable to those by MODTRAN 5. However, the proposed method required further improvements particularly for high-observation angle conditions. Actual effects of the parameter calculation errors could be indirectly recognized by the estimation result of SST estimated. The results of SST estimation showed that that accuracy of the proposed method was comparable to that of other multi-channel-based methods. Especially, the SST estimation of the proposed method from the MWIR region (VIIRS I4) resulted in a difference of 0.03 in both the squared correlation coefficient  $R^2$  and RMSE, which was comparable to the multi-channel method-based VIIRS SST product (Table 4). The results from the TIR region (VIIRS I5) showed the largest RMSE, which would be caused by errors in the atmospheric correction parameter calculations (Table 4). In addition, the results of the MWIR region for the daytime images were not presented in this study because they were seriously affected by solar irradiance. The daytime MWIR results after a simple Sun-glint correction process will be introduced in further studies.

### 4.2. Effects of Observation Angles

Figure 11 shows the error in SST estimation by the proposed method according to various satellite observation angles during the nighttime. The fitted lines indicate their trends. All I4 and I5 derived results in Figure 11a,b had slopes smaller than the  $10^{-2}$  order, which was comparable to that of VIIRS or the MODIS SST product. This clearly demonstrated that the proposed single-channel method was free from angular dependency on SST estimation up to a  $60^\circ$  observation angle. This suggested that the correction functions for angular effects (Equations (17) to (19)) compensated the effects of observation angles.

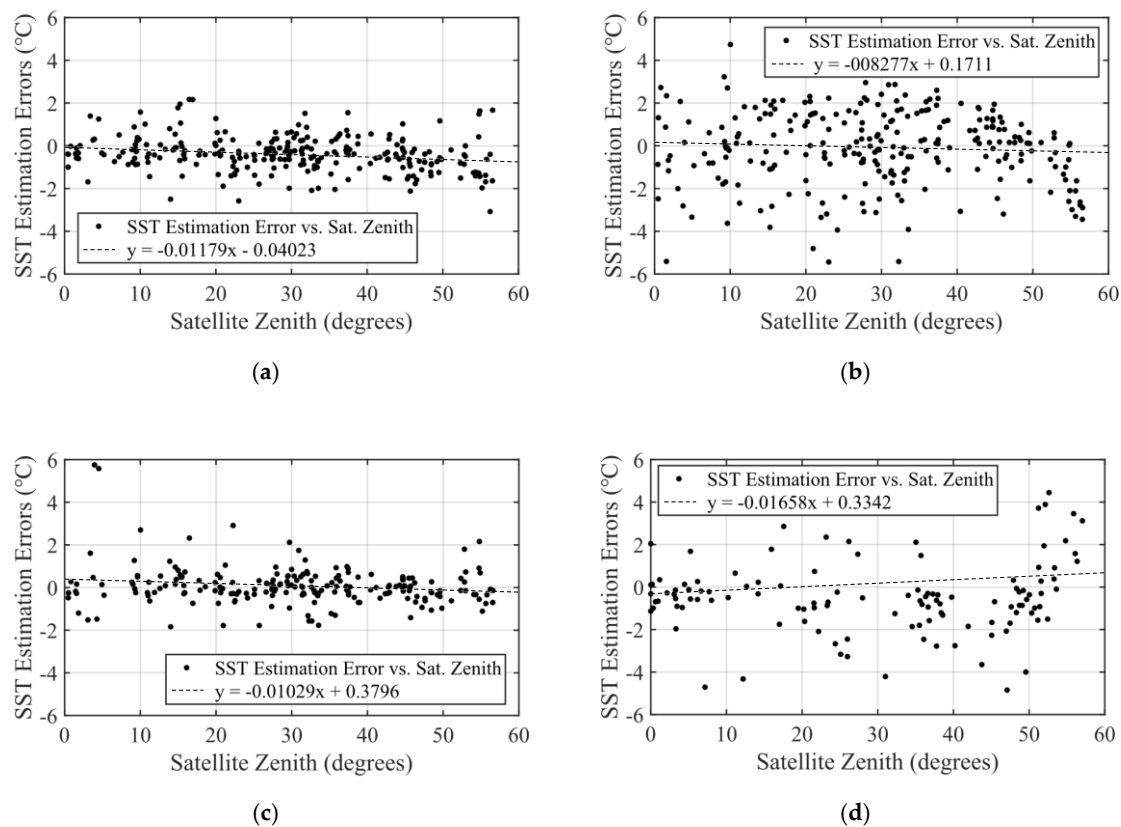


**Figure 11.** Error distributions of SST estimations with the proposed method and their trends according to various satellite and observation angles: (a) derived from the VIIRS I4 band, (b) derived from the VIIRS I5 band, (c) VIIRS SST product, and (d) MODIS SST product [29,30].

4.3. Effects of Selecting Numerical Prediction Models between LDAPS and RDAPS

The effects of numerical model spatial resolutions were also assessed based on estimated SSTs (Table 5). Two types of weather prediction models were used, as described in Section 2.1, including the RDAPS with a resolution of 12 km and the LDAPS with a resolution of 1.5 km. The results are listed in Table 5. Even with a low spatial resolution of 12 km, the estimation errors of the I4 derived SSTs were comparable to those obtained by using a model of higher spatial resolution. For instance, RMSE of the I4 band increased from 0.95 °C to 0.99 °C, while the maximum error decreased from 3.80 °C to 3.67 °C. However, for the TIR region, errors decreased coherently as the spatial resolution of the numerical model increased, except for the mean error.

**Table 5.** Errors of SSTs derived from VIIRS imaging channels with the proposed single-channel atmospheric correction method for comparison between different weather prediction models having different spatial resolutions.

Errors ( °C) and Systems	LDAPS (1.5 km Resolution)			
	Mean	Std.	Max.	RMSE
VIIRS I4 band	-0.23	0.96	3.67	0.99
VIIRS I5 band	0.98	1.01	3.16	1.41
Errors ( °C) and Systems	RDAPS (12 km Resolution)			
	Mean	Std.	Max.	RMSE
VIIRS I4 band	-0.39	0.86	3.86	0.95
VIIRS I5 band	-0.07	1.80	6.39	1.81

To cover the area displayed in Figure 9 and Table 3, in total, 1,920,000 pixels (1200 pixels by 1600 pixels) were required for LDAPS data. Meanwhile, only 28,000 pixels (200 pixels by 140 pixels) of RDAPS data could cover the same area. The calculation time of the proposed model depended on the number of atmospheric layers, the amount of NWP data, and computing power. For calculations with 2000 atmospheric layers (for MWIR images), it took about 3 h to process using LDAPS data and about 2 h using RDAPS data. With 300 layers (for LWIR images), it took about 30 min using LDAPS data and about 20 min using RDAPS data. The calculation time of conventional radiative transfer codes also depended on conditions and simulation settings. However, an assumption of just 0.5 s per calculation would result in about 4 h, for calculations on every 28,000 pixels in RDAPS data. Furthermore, calculations using LDAPS data would cost about 267 h.

Therefore, according to this brief comparison in this study, a consistent improvement of SST estimation errors could not be recognized, despite a spatial resolution improvement of NWP data and an increase of the calculation time. This implied that inhomogeneity of atmospheric components affecting infrared atmospheric correction would be negligible within the 12 km range and over a sea surface.

## 5. Conclusions

This study proposed a single-channel atmospheric correction algorithm for both mid-wavelength and thermal infrared channels. The proposed algorithm utilized high spatial resolution NWP models for infrared atmospheric correction. It re-organized atmospheric profiles according to each pixel of the NWP models within the infrared images, accounting for their viewing geometry. Therefore, it was applicable to sensors with a wide field of view or sensors with a high maneuver and various observation angles. It adopted an absorption-focused regression model and basic radiative transfer equations to simplify the calculations. This approach could achieve a simple deduction of atmospheric optical thickness and the calculation of atmospheric correction parameters, and consequently, the atmospheric correction parameters for every pixel of NWP data could be calculated with a single step calculation.

The proposed method was applied to VIIRS I4 and I5 bands for estimating SSTs and its validation. SSTs estimated around the Korean Peninsula were compared with sea-truth temperatures from ocean buoys for validation. SST products of VIIRS and MODIS, which were based on multi-channel methods, were also used for comparison.

From the results of SST estimation, the proposed method applied to satellite infrared images showed a comparable accuracy to the widely used RTM, MODTRAN 5, or even multi-channel-based atmospheric correction algorithms (VIIRS/MODIS SST products) during the nighttime. In addition, estimation errors were almost independent of observation angles up to 60°. These validation results supported that the proposed method using high-resolution NWP models was effectively able to conduct an atmospheric correction for various observation angles.

The KMA NWP models used in this study had specific boundaries of data, which restricted the validation area of the algorithm. Nevertheless, utilization examples of high-resolution NWP models, combined with a simplified radiative transfer model, were provided under this study. The results and approach of this study will be a helpful background for studies combining high-resolution NWP models and infrared satellite imagery.

**Author Contributions:** Conceptualization, H.L. and W.P.; methodology, H.L.; software, H.L.; validation, H.L., W.P. and J.-S.W.; formal analysis, H.L.; investigation, H.L. and W.P.; resources, H.L., W.P. and J.-S.W.; data curation, W.P.; writing—original draft preparation, H.L.; writing—review and editing, H.L., W.P. and J.-S.W.; visualization, H.L.; supervision, J.-S.W.; project administration, W.P.; funding acquisition, J.-S.W. All authors have read and agreed to the published version of the manuscript.

**Funding:** This work was supported by the Korea Meteorological Administration Research and Development Program under grant KMI2018-02910.

**Acknowledgments:** This work was supported by the Korea Meteorological Administration Research and Development Program under grant KMI2018-02910.

**Conflicts of Interest:** The funders had no role in the design of the study; in the collection, analyses, or interpretation of data; in the writing of the manuscript, or in the decision to publish the results.

## References

1. Wan, Z.; Dozier, J. A generalized split-window algorithm for retrieving land-surface temperature from space. *IEEE Trans. Geosci. Remote Sens.* **1996**, *34*, 892–905.
2. Jiménez-Muñoz, J.C.; Sobrino, J.A. A generalized single-channel method for retrieving land surface temperature from remote sensing data. *J. Geophys. Res. Atmos.* **2003**, *108*, 4688–4695. [[CrossRef](#)]
3. Li, F.; Jackson, T.J.; Kustas, W.P.; Schmugge, T.J.; French, A.N.; Cosh, M.H.; Bindlish, R. Deriving land surface temperature from Landsat 5 and 7 during SMEX02/SMACEX. *Remote Sens. Environ.* **2004**, *92*, 521–534. [[CrossRef](#)]
4. Jiménez-Muñoz, J.C.; Cristóbal, J.; Sobrino, J.A.; Sòria, G.; Ninyerola, M.; Pons, X. Revision of the single-channel algorithm for land surface temperature retrieval from Landsat thermal-infrared data. *IEEE Trans. Geosci. Remote Sens.* **2009**, *47*, 339–349. [[CrossRef](#)]
5. Tang, H.; Li, Z.L. *Quantitative Remote Sensing in Thermal Infrared: Theory and Applications*; Springer Science & Business Media: Berlin, Germany, 2013; pp. 13–25, 93–135, ISBN 978-3-642-42027-6.
6. Ulivieri, C.M.M.A.; Castronuovo, M.M.; Francioni, R.; Cardillo, A. A split window algorithm for estimating land surface temperature from satellites. *Adv. Space Res.* **1994**, *14*, 59–65. [[CrossRef](#)]
7. Yu, X.; Guo, X.; Wu, Z. Land surface temperature retrieval from Landsat 8 TIRS—Comparison between radiative transfer equation-based method, split window algorithm and single channel method. *Remote Sens.* **2014**, *6*, 9829–9852. [[CrossRef](#)]
8. Zheng, X.; Li, Z.L.; Nerry, F.; Zhang, X. A new thermal infrared channel configuration for accurate land surface temperature retrieval from satellite data. *Remote Sens. Environ.* **2019**, *231*, 111216. [[CrossRef](#)]
9. Zhang, S.; Duan, S.B.; Li, Z.L.; Huang, C.; Wu, H.; Han, X.J.; Gao, M. Improvement of Split-Window Algorithm for Land Surface Temperature Retrieval from Sentinel-3A SLSTR Data Over Barren Surfaces Using ASTER GED Product. *Remote Sens.* **2019**, *11*, 3025. [[CrossRef](#)]
10. Barsi, J.A.; Schott, J.R.; Palluconi, F.D.; Helder, D.L.; Hook, S.J.; Markham, B.L.; Chander, G.; O'Donnell, E.M. Landsat TM and ETM+ thermal band calibration. *Can. J. Remote Sens.* **2003**, *29*, 141–153. [[CrossRef](#)]
11. Wang, M.; Zhang, Z.; Hu, T.; Liu, X. A practical single-channel algorithm for land surface temperature retrieval: Application to Landsat series data. *J. Geophys. Res. Atmos.* **2019**, *124*, 299–316. [[CrossRef](#)]
12. Jiménez-Muñoz, J.C.; Sobrino, J.A. A single-channel algorithm for land-surface temperature retrieval from ASTER data. *IEEE Geosci. Remote Sens. Lett.* **2010**, *7*, 176–179. [[CrossRef](#)]
13. Cristóbal, J.; Jiménez-Muñoz, J.C.; Prakash, A.; Mattar, C.; Skoković, D.; Sobrino, J.A. An Improved Single-Channel Method to Retrieve Land Surface Temperature from the Landsat-8 Thermal Band. *Remote Sens.* **2018**, *10*, 431. [[CrossRef](#)]
14. Barsi, J.A.; Barker, J.L.; Schott, J.R. An atmospheric correction parameter calculator for a single thermal band earth-sensing instrument. In Proceedings of the IGARSS 2003, Toulouse, France, 21–25 July 2003; IEEE Cat. No. 03CH37477. Volume 5, pp. 3014–3016.
15. Srivastava, P.K.; Han, D.; Rico-Ramirez, M.A.; Bray, M.; Islam, T.; Gupta, M.; Dai, Q. Estimation of land surface temperature from atmospherically corrected LANDSAT TM image using 6S and NCEP global reanalysis product. *Environ. Earth Sci.* **2014**, *72*, 5183–5196. [[CrossRef](#)]
16. Tardy, B.; Rivalland, V.; Huc, M.; Hagolle, O.; Marcq, S.; Boulet, G. A software tool for atmospheric correction and surface temperature estimation of Landsat infrared thermal data. *Remote Sens.* **2016**, *8*, 696. [[CrossRef](#)]
17. Islam, T.; Hulley, G.C.; Malakar, N.K.; Radocinski, R.G.; Guillevic, P.C.; Hook, S.J. A physics-based algorithm for the simultaneous retrieval of land surface temperature and emissivity from VIIRS thermal infrared data. *IEEE Trans. Geosci. Remote Sens.* **2017**, *55*, 563–576. [[CrossRef](#)]
18. Cao, C.; Xiong, J.; Blonski, S.; Liu, Q.; Urety, S.; Shao, X.; Bai, Y.; Weng, F. Suomi NPP VIIRS sensor data record verification, validation, and long-term performance monitoring. *J. Geophys. Res. Atmos.* **2013**, *118*, 11–664. [[CrossRef](#)]
19. Korea Meteorological Administration (KMA). *Application Manual of Numerical Forecast Data*; Korea Meteorological Administration (KMA): Seoul, Korea, 2013.

20. Liou, K.N. *An Introduction to Atmospheric Radiation*, 2nd ed.; Elsevier: Amsterdam, The Netherlands, 2002; pp. 116–168, ISBN 978-0-12-451451-5.
21. Meador, W.E.; Weaver, W.R. Two-stream approximations to radiative transfer in planetary atmospheres: A unified description of existing methods and a new improvement. *J. Atmos. Sci.* **1980**, *37*, 630–643. [[CrossRef](#)]
22. Lee, K.M. *Atmospheric Radiation*, 1st ed.; Sigma Press: Seoul, Korea, 2000; pp. 23–31, 109–132, ISBN 89-8445-037-5.
23. Griffin, M.K.; Hsiao-hua, K.B.; Kerekes, J.P. Understanding radiative transfer in the midwave infrared: A precursor to full-spectrum atmospheric compensation. In Algorithms and Technologies for Multispectral, Hyperspectral, and Ultraspectral Imagery X. *Int. Soc. Opt. Photonics* **2004**, *5425*, 348–357.
24. Saunders, R.; Hocking, J.; Turner, E.; Rayer, P.; Rundle, D.; Brunel, P.; Vidot, J.; Roquet, P.; Matricardi, M.; Geer, A.; et al. An update on the RTTOV fast radiative transfer model (currently at version 12). *Geosci. Model Dev.* **2018**, *11*, 2717–2737. [[CrossRef](#)]
25. Carmichael, R. *Geopotential and Geometric Altitude*; Public Domain of Aeronautical Software (PDA): Santa Cruz, CA, USA, 2003.
26. Nicolòs, R.; Caselles, V.; Valor, E.; Coll, C.; Sanchez, J.M. A simple equation for determining sea surface emissivity in the 3–15  $\mu$  m region. *Int. J. Remote Sens.* **2009**, *30*, 1603–1619. [[CrossRef](#)]
27. Baldridge, A.M.; Hook, S.J.; Grove, C.I.; Rivera, G. The ASTER Spectral Library Version 2.0. *Remote Sens. Environ.* **2009**, *113*, 711–715. [[CrossRef](#)]
28. Korea Meteorological Administration (KMA). *Explanation Document of Meteorological Data; Marine Weather Buoys, Wave Height Buoys, Marine Light Beacons*; Korea Meteorological Administration (KMA): Seoul, Korea, 2015.
29. NOAA Office of Satellite and Product Operations (OSPO). *GHRSSST GDS2 Level 2P Global Skin Sea Surface Temperature from the Visible Infrared Imaging Radiometer Suite (VIIRS) on the Suomi NPP satellite created by the NOAA Advanced Clear-Sky Processor for Ocean (ACSP0)*; Ver. 2.4; PO.DAAC: Pasadena, CA, USA, 2015. [[CrossRef](#)]
30. JPL/OBPG/RSMAS. *GHRSSST Level 2P Global Skin Sea Surface Temperature from the Moderate Resolution Imaging Spectroradiometer (MODIS) on the NASA Aqua Satellite*; Ver. 2014.0; PO.DAAC: Pasadena, CA, USA, 2016. [[CrossRef](#)]



© 2020 by the authors. Licensee MDPI, Basel, Switzerland. This article is an open access article distributed under the terms and conditions of the Creative Commons Attribution (CC BY) license (<http://creativecommons.org/licenses/by/4.0/>).